

₁ Physics-Infused Reduced-Order Modeling for Analysis of
₂ Ablating Hypersonic Thermal Protection Systems

₃

₄ November 11, 2025

₅ **Abstract**

This work presents a *physics-infused reduced-order modeling* (PIROM) framework towards the design, analysis, and optimization of non-decomposing ablating hypersonic thermal protection systems (TPS). It is demonstrated via the modeling of transient thermo-ablative behavior of non-decomposing multi-layered hypersonic TPS. The PIROM architecture integrates a reduced-physics backbone, based on the lumped-capacitance model (LCM), with data-driven correction dynamics formulated via a coarse-graining approach rooted in the Mori-Zwanzig formalism. The LCM is coupled to a surface velocity model (SVM) to capture the recession of the ablating TPS as a function of the surface temperature. While the LCM and SVM capture the dominant physics of the ablating TPS response, the correction terms compensate for residual dynamics arising from higher-order non-linear interactions and heterogeneities across material layers. The PIROM consistently achieves errors below 1% for a wide range of extrapolative settings of design parameters involving time-and-space varying boundary conditions and SVM models, and improves by $x\%$ over the LCM alone. Moreover, the PIROM delivers online evaluations that are two orders of magnitude faster than the full-order model (FOM). These results demonstrate that PIRO effectively reconciles the trade-offs between accuracy, generalizability, and efficiency, providing a promising framework for optimizing multi-physical dynamical systems, such as TPS under diverse operating conditions.

₂₅ **1 Introduction**

₂₆ At hypersonic speeds, aerospace vehicles experience extreme aero-thermo-dynamic environments that require specialized thermal protection systems (TPS) to shield internal sub-
₂₇ structures, electronics, and possibly crew members from the intense aerodynamic heating.
₂₈

29 The TPS is often composed of ablating materials – a high-temperature capable fibrous
30 material injected with a resin that fills the pore network and strengthens the composite
31 [Amar2016](#). The TPS design promotes the exchange of mass through thermal and
32 chemical reactions (i.e., pyrolysis), effectively mitigating heat transfer to the sub-structures.

33 As a result, accurate prediction for the ablating TPS response under extreme hyper-
34 sonic heating becomes fundamental to ensuring survivability, performance, and safety of
35 hypersonic vehicles. Not only is it necessary to assess the performance of the thermal man-
36 agement systems, but also the shape changes of the vehicle’s outer surface induced by the
37 ablating material, and its impact on the aerodynamics, structural integrity, and controlla-
38 bility. Nonetheless, high-fidelity simulations of ablating TPS remains a formidable challenge
39 both theoretically and computationally.

40 Unfortunately, high-fidelity simulations of ablating TPS remains a formidable challenge
41 both theoretically and computationally.

42 On the theoretical side, the thermo-chemical reactions, coupled with the irregular pore
43 network structure, translate into simplifying assumptions to reduce non-linearities, and make
44 the resulting equations more amenable for engineering application and design analysis [x](#).
45 For instance, one of the most notable codes is the one-dimensional [CMA](#) code that was
46 developed by Aerotherm Corporation in the 1960s [Howard2015](#). Despite its practical use
47 in...

48 Another example is the CHarring Ablator Response (CHAR) ablation code, which ignores
49 elemental decompositions of the pyrolyzing gases, assumes the gases to be a mixture of perfect
50 gases in thermal equilibrium, and assumes no reaction or condensation with the porous
51 network [1].

52 [theoretically:](#)

53 [computationally:](#)

54 2 Modeling of Ablating Thermal Protection Systems

55 This section presents the problem of modeling a non-decomposing ablating TPS subjected to
56 extreme hypersonic heating. Two different but mathematically connected solution strategies
57 are provided: (1) a high-fidelity full-order model (FOM) based on a finite element method
58 (FEM), and (2) a low-fidelity reduced-physics model (RPM) based on a lumped capacitance
59 model (LCM) and a one-dimensional surface velocity model (SVM). The FOM is compu-
60 tationally expensive but provides the highest fidelity, while the RPM is computationally
61 efficeint but has low predictive fidelity; both models are amenable to high-dimensional de-
62 sign variables. The RPM is used in the subsequent sections for deriving the PIROM.

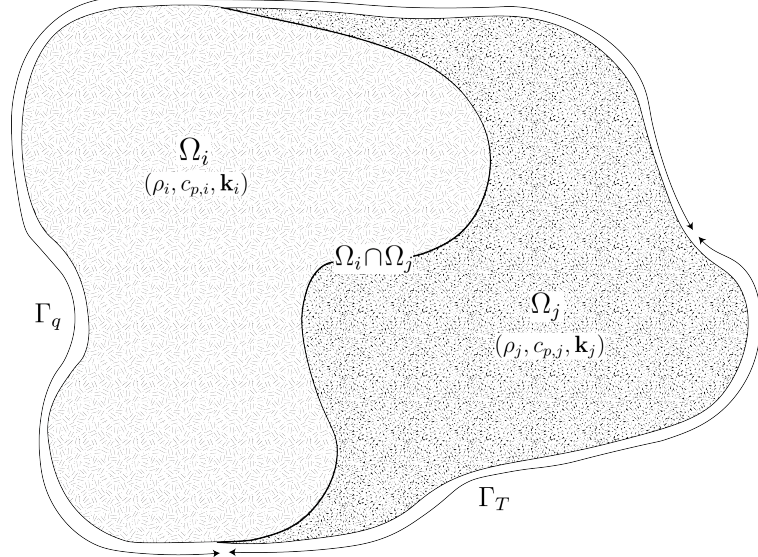


Figure 1: General domain Ω with prescribed Neumann and Dirichlet boundary conditions on Γ_q and Γ_T . Mesh displacement $w(x, t)$ occurs on the Γ_q boundary.

63 2.1 Governing Equations

64 The multi-physics for a non-decomposing ablating TPS involves the *energy equation* which
 65 models the transient heat conduction inside the TPS, and the *pseudo-elasticity equation*,
 66 which models the mesh motion due to surface recession. The governing PDEs for the ablating
 67 TPS are summarized in this section.

68 **Energy Equation** Consider a generic domain $\Omega \subset \mathbb{R}^d$, $d = 2$ or 3 , illustrated in Fig. 1. Let
 69 $\partial\Omega = \Gamma_q \cup \Gamma_T$ and $\Gamma_q \cap \Gamma_T = \emptyset$, where a Neumann $q_b(x, t)$ boundary condition is prescribed
 70 on the Γ_q boundary, and represents the surface exposed to the hypersonic boundary layer.
 71 The Dirichlet $T_b(x, t)$ boundary condition is prescribed on the boundary Γ_T . The TPS is
 72 divided into N non-overlapping components $\{\Omega_i\}_{i=1}^N$, as illustrated in Fig. 1 for $N = 2$. The
 73 i -th component Ω_i is associated with material properties $(\rho^{(i)}, c_p^{(i)}, \mathbf{k}^{(i)})$, that are assumed
 74 to be continuous within one component, and can be discontinuous across two neighboring
 75 components.

76 The transient heat conduction is described by the energy equation,

$$\rho c_p \left(\frac{\partial T}{\partial t} + \tilde{\mathbf{v}}(x, t) \cdot \nabla T \right) - \nabla \cdot (\mathbf{k} \nabla T) = 0, \quad x \in \Omega \quad (1a)$$

$$-\mathbf{k} \nabla T \cdot \mathbf{n} = q_b(x, t), \quad x \in \Gamma_q \quad (1b)$$

$$T(x, t) = T_b(x, t), \quad x \in \Gamma_T \quad (1c)$$

$$T(x, 0) = T_0(x), \quad x \in \Omega \quad (1d)$$

77 where the density ρ is constant, while the heat capacity c_p and thermal conductivity $\mathbf{k} \in \mathbb{R}^{d \times d}$
78 may depend on temperature. In the order they appear, the terms in eq. (1a) include, the
79 unsteady energy storage, heat conduction, temperature advection due to mesh motion, and
80 source terms due to boundary conditions. The boundary conditions for the energy equation
81 includes Neumann eq. (1b) on Γ_1 and Dirichlet eq. (1c) on Γ_T .

82 An Abirtrary Lagrangian-Eulerian (ALE) description is used to account for mesh motion
83 due to surface recession, where $\tilde{\mathbf{v}}(x, t)$ is the relative velocity of the material with respect to
84 the mesh,

$$\tilde{\mathbf{v}}(x, t) = \mathbf{v}_s(x, t) - \mathbf{v}_m(x, t) \quad (2)$$

85 where $\mathbf{v}_s(x, t)$ and $\mathbf{v}_m(x, t)$ are the physical material velocity and mesh velocity, respectively.
86 For ablating TPS, the physical material velocity is assumed to be zero, i.e., $\mathbf{v}_s(x, t) = \mathbf{0}$, and
87 thus the relative velocity is simply the negative of the mesh velocity, $\tilde{\mathbf{v}}(x, t) = -\mathbf{v}_m(x, t)$.

88 **Pseudo-Elasticity Equation** The mesh motion is described by the steady-state pseudo-
89 elasticity equation without body forces,

$$\nabla \cdot \boldsymbol{\sigma}(\mathbf{w}) = \mathbf{0}, \quad \forall t \in \mathcal{T}, \quad \mathbf{x} \in \Omega \quad (3a)$$

$$\mathbf{w}(\mathbf{x}, t) = \mathbf{w}_q(\mathbf{x}, t), \quad \forall t \in \mathcal{T}, \quad \mathbf{x} \in \Gamma_q \quad (3b)$$

$$\mathbf{w}(\mathbf{x}, t) = \mathbf{0}, \quad \forall t \in \mathcal{T}, \quad \mathbf{x} \notin \Gamma_q \quad (3c)$$

$$\mathbf{w}(\mathbf{x}, 0) = \mathbf{0}, \quad \forall \mathbf{x} \in \Omega \quad (3d)$$

90 where the stress tensor $\boldsymbol{\sigma}$ is related to the strain tensor $\boldsymbol{\epsilon}(\mathbf{w})$ through Hooke's law,

$$\boldsymbol{\sigma}(\mathbf{w}) = \mathbb{D} : \boldsymbol{\epsilon}(\mathbf{w})$$

91 where \mathbb{D} is the fourth-order positive definite elasticity tensor, and “ $:$ ” is the double con-
92 traction of the full-order tensor \mathbb{D} with the second-order tensor $\boldsymbol{\epsilon}$. The elasticity tensor
93 ordinarily possess a number of symmetries, effectively reducing the number of components

94 that describe it [2]. The symmetric strain tensor ϵ measures the deformation of the mesh
 95 due to displacements $\mathbf{w}(x, t)$, and is defined as,

$$\epsilon(\mathbf{w}) = \frac{1}{2} (\nabla \mathbf{w} + \nabla \mathbf{w}^T)$$

96 The “material” properties for the mesh are chosen to tailor the mesh deformation, and need
 97 not represent the actual material being modeled [1].

98 For the pseudo-elasticity equations, the boundary conditions include prescribed displace-
 99 ments $\mathbf{w}_q(x, t)$ on the heated boundary Γ_q in eq. (3b), and zero displacements on the unheated
 100 boundaries in eq. (3c). The initial condition for the mesh displacements is zero in eq. (3d).
 101 Particularly, the surface velocity due to the ablating material is a function of the surface
 102 temperature $T_q(x, t)$ for $x \in \Gamma_q$ on the heated boundary. For the i -th material component,
 103 the surface velocity is imposed based on the following relation,

$$\hat{\mathbf{n}} \cdot \mathbf{v}_m(x, t) = f(T_q(x, t)), \quad x \in \Gamma_q \quad (4)$$

104 where $\hat{\mathbf{n}}$ is the unit normal vector on the heated boundary Γ_q , and f is a function obtained
 105 from tabulated data for the material, commonly referred to as a B' table [1]. The B' table
 106 provides the recession velocity as a function of surface temperature, and is pre-computed
 107 based on high-fidelity simulations of the ablation process for a one-dimensional slab of the
 108 material, and is independent of the TPS geometry and boundary conditions. The surface
 109 displacements correspond to the boundary

110 are then computed by integrating the surface velocities over time,

$$\mathbf{w}_q(x, t) = \int_0^t \mathbf{v}_m(x, \tau) d\tau \quad (5)$$

111 2.2 Full-Order Model: Finite-Element Method

112 To obtain the full-order numerical solution, the governing equation is spatially discretized
 113 using variational principles of Discontinuous Galerkin (DG) to result in a high-dimensional
 114 system of ordinary differential equations (ODEs). Note that the choice of DG approach here
 115 is mainly for theoretical convenience in the coarse-graining formulation, and is exclusively
 116 performed on the energy equation as the quantities of interest correspond to the ablating
 117 surface temperatures. In Sec. **x**, the high-fidelity ablating TPS solution is performed using
 118 standard FEM for both the energy and elasticitiy equations, and the equivalence between
 119 DG and standard FEM is noted upon their convergence.

120 Consider a conforming mesh partition domain, where each element belongs to one and

121 only one component. Denote the collection of all M elements as $\{E_i\}_{i=1}^M$. In an element E_i ,
122 its shared boundaries with another element E_j , Neumann BC, and Dirichlet BC are denoted
123 as e_{ij} , e_{iq} , and e_{iT} , respectively. Lastly, $|e|$ denotes the length ($n_d = 2$) or area ($n_d = 3$) of a
124 component boundary e .

125 For the i -th element, use a set of P trial functions, such as polynomials, to represent the
126 temperature distribution,

$$T^{(i)}(x, t) = \sum_{l=1}^P \phi_l^{(i)}(x) u_l^{(i)} \equiv \boldsymbol{\phi}^{(i)}(x)^T \mathbf{u}^{(i)}(t), \quad i = 1, 2, \dots, M \quad (6)$$

127 By standard variational processes, e.g., [Cohen2018](#), the element-wise governing equation is
128 denoted as,

$$\mathbf{A}^{(i)} \dot{\mathbf{u}}^{(i)} = (\mathbf{B}^{(i)} + \mathbf{C}^{(i)}) \mathbf{u}^{(i)} + \sum_{j \in \mathcal{N}_i \cup \{T_b\}} (\mathbf{B}_{ij}^{(i)} \mathbf{u}^{(i)} + \mathbf{B}_{ij}^{(j)} \mathbf{u}^{(j)}) + \mathbf{f}^{(i)}(t), \quad \text{for } i = 1, 2, \dots, M \quad (7)$$

129 which is collected as the following ODE for the all the elements in the mesh,

$$\mathbf{A}(\mathbf{u}) \dot{\mathbf{u}} = [\mathbf{B}(\mathbf{u}) + \mathbf{C}(\mathbf{u})] \mathbf{u} + \mathbf{f}(t) \quad (8)$$

130 where $\mathbf{u} = [\mathbf{u}^{(1)}, \mathbf{u}^{(2)}, \dots, \mathbf{u}^{(M)}]^T \in \mathbb{R}^{MP}$ includes all the DG variables, $\mathbf{f} \in \mathbb{R}^{MP}$ is the
131 external forcing, and the system matrices \mathbf{A} , \mathbf{B} , and \mathbf{C} are the matrices due to heat capacity,
132 heat conduction, and temperature advection due to mesh motion, respectively. A detailed
133 derivation of eqs. (7) and (8) and their matrices is provided in Appendix [?].

134 2.3 Reduced-Physics Model

135 The RPM for predicting the response of the ablating TPS consists of two components: (1) the
136 LCM, and (2) tabulated data for ablating velocity as a function of surface temperature. The
137 LCM is described as a first-order system of ODEs for predicting the average temperatures
138 inside the ablating TPS, and provides a low-fidelity under-estimation for the ablating surface
139 temperature. The temperature prediction from LCM is used in a B' table to determine the
140 surface recession velocity, from which the displacements are obtained through integration.

141 2.3.1 Lumped Capacitance Model

142 The main results regarding the LCM are provided in this section; details of the implementa-
143 tion for the TPS in Fig. 2 are provided in Appendix A. The LCM is a classical physics-based

¹⁴⁴ low-order model for predicting the temporal variation of average temperature in multiple in-
¹⁴⁵ terconnected components INCROPERA. The LCM is derived at the component level from
¹⁴⁶ a point of view of energy conservation, and leads to the following system of ODEs for the
¹⁴⁷ average temperatures on the components,

$$\bar{\mathbf{A}} \dot{\bar{\mathbf{u}}} = \bar{\mathbf{B}}(\bar{\mathbf{u}}) \bar{\mathbf{u}} + \bar{\mathbf{f}}(t) \quad (9)$$

¹⁴⁸ where,

$$\bar{\mathbf{u}} = [\bar{u}^{(1)}, \bar{u}^{(2)}, \dots, \bar{u}^{(N)}]^T \in \mathbb{R}^N \quad (10a)$$

$$\bar{\mathbf{f}} = [\bar{f}^{(1)}, \bar{f}^{(2)}, \dots, \bar{f}^{(N)}]^T \in \mathbb{R}^N \quad (10b)$$

¹⁴⁹ includes the average temperatures $\bar{\mathbf{u}}$ and forcing inputs $\bar{\mathbf{f}}$ for the N components. For $i, j =$
¹⁵⁰ $1, 2, \dots, N$ the (i, j) -th elements of the $\bar{\mathbf{A}} \in \mathbb{R}^{N \times N}$, $\bar{\mathbf{B}} \in \mathbb{R}^{N \times N}$, and $\bar{\mathbf{f}} \in \mathbb{R}^N$ matrices are
¹⁵¹ given by,

$$\bar{A}^{(i)} = \begin{cases} \int_{\Omega^{(i)}} \rho c_p d\Omega^{(i)}, & i = j \\ 0, & i \neq j \end{cases}, \quad \bar{B}_{ij} = \begin{cases} \sum_{j \in \mathcal{N}_i \cup \{T_b\}} \bar{B}_{ij}^{(i)}, & i = j \\ \bar{B}_{ij}^{(j)}, & i \neq j \end{cases}, \quad (11a)$$

$$\mathbf{f}^{(i)} = \begin{cases} |e_{iq}| \bar{q}^{(i)} + \frac{|e_{iT}|}{R_i} \bar{T}^{(i)}, & i = j \\ 0, & i \neq j \end{cases} \quad (11b)$$

¹⁵² where,

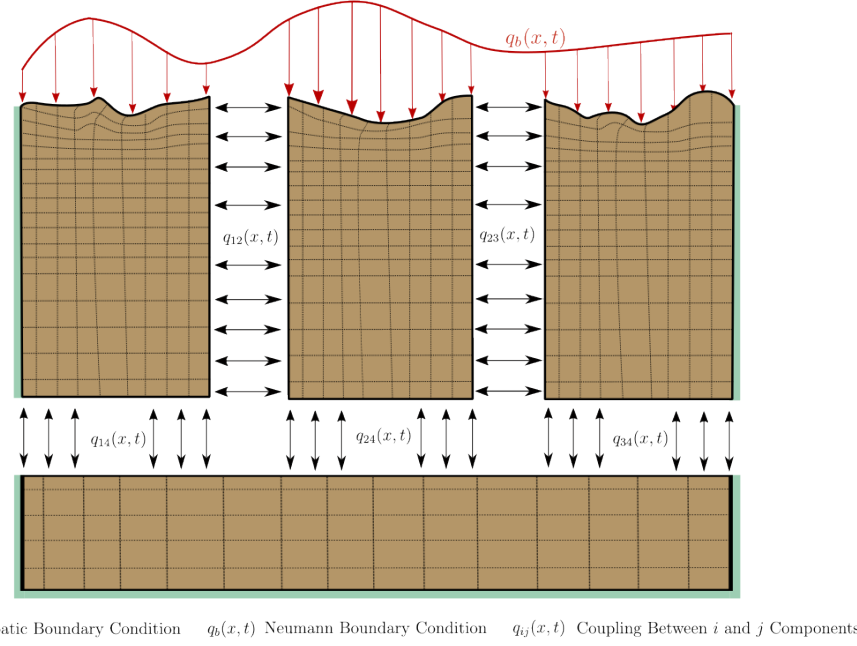
$$\bar{q}^{(i)} = \frac{1}{|e_{iq}|} \int_{e_{iq}} q_b d e_{iq}, \quad \bar{T}^{(i)} = \frac{1}{|e_{iT}|} \int_{e_{iT}} T_b d e_{iT}, \quad \bar{B}_{ij}^{(i)} = -\frac{|e_{ij}|}{R_{ij}}, \quad \bar{B}_{ij}^{(j)} = \frac{|e_{ij}|}{R_{ij}} \quad (12)$$

¹⁵³ 2.3.2 Surface Recession Velocity and Displacements

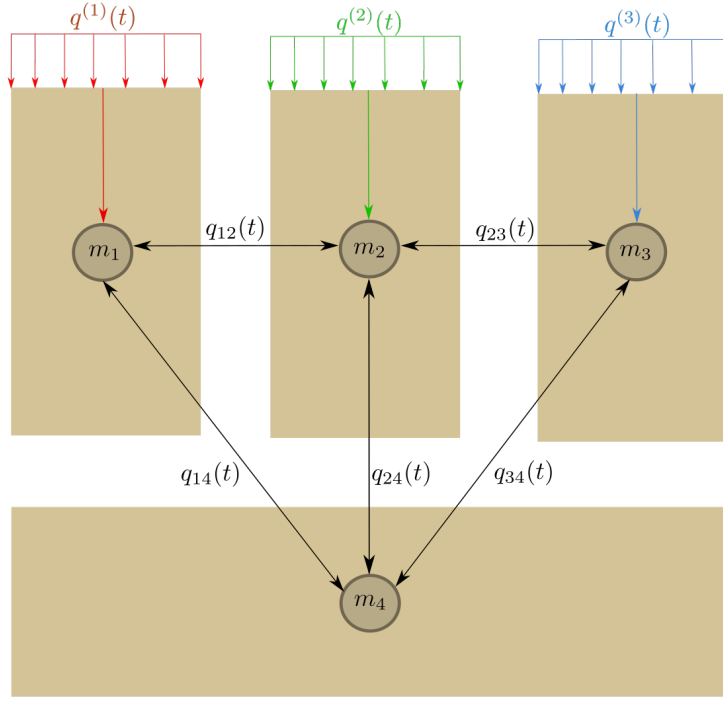
¹⁵⁴ The surface velocity on the heated boundary Γ_q is computed based on the temperature
¹⁵⁵ predicted by the LCM using eq. (4). Thus, based on the i -th average temperature $\bar{u}^{(i)}$, the
¹⁵⁶ wall-normal surface velocity is computed as,

$$\hat{\mathbf{n}} \cdot \mathbf{v}^{(i)}(x, t) = f(\bar{u}^{(i)}(t)) \quad (13)$$

¹⁵⁷ Due



(a) TPS Decomposition



(b) Lumped Mass Representation

Figure 2: Partition of the TPS into three ablating and one non-ablating components with the corresponding lumped-mass representation.

158 **2.4 Summary of Modeling Approaches**

159 The FOM (i.e., DG-FEM) and RPM (i.e., LCM) are two different but mathematically con-
160 nected solution strategies. Specifically, the LCM in eq. (9) not only resembles the functional
161 form of the DG model in eq. (8), but can be viewed as a special case of the latter, where the
162 mesh partition is extremely coarse, and the trial and test functions are piece-wise constants.
163 For example, consider the case where each component $\Omega^{(i)}$ is treated as one single element,
164 and each element employs one constant basis function $\phi^{(i)} = 1$. The element-wise DG model
165 in eq. (7) simplifies into a scalar ODE that ignores advection effects due to mesh motion,

$$\mathbf{A}^{(i)} = \bar{A}^{(i)}, \quad \mathbf{C}^{(i)} = 0, \quad \mathbf{B}_{ij}^{(i)} = -\sigma|e_{ij}|, \quad \mathbf{B}_{ij}^{(j)} = \sigma|e_{ij}|, \quad \mathbf{f}^{(i)} = |e_{iq}|\bar{q}^{(i)} + \sigma|e_{iT}|\bar{T}^{(i)} \quad (14)$$

166 Clearly, the LCM is a coarse zeroth-order DG model with the inverse of thermal resistance
167 chosen as the element-wise penalty factors. Or conversely, the DG model is a refined version
168 of LCM via *hp*-adaptation.

169 The FOM and RPM represent two extremes in the modeling fidelity and computational
170 cost spectrum. On one hand, the FOM is the most accurate but computationally expensive
171 to evaluate due to the fine mesh discretizations for both the temperature and displacement
172 fields, leading to possibly millions of state variables. On the other hand, the RPM considers
173 only the average temperature of the material as the state variable, considerably reducing
174 the computational cost, but sacrificing local temperature information and thus neglecting
175 higher-order effects due to mesh motion. Thus, neither the FOM nor the RPM is a universal
176 approach for real-world analysis, design, and optimization tasks for ablating TPS, where
177 thousands of high-fidelity model evaluations may be necessary. This issue motivates the
178 development of the PIROM, which can achieve the fidelity of FOM at a computational cost
179 close to the RPM, while maintaining the generalizability to model parameters.

180 **3 Physics-Infused Reduced-Order Modeling**

181 The formulation of PIROM for ablating TPS starts by connecting the FOM, i.e., DG-FEM,
182 and the RPM, i.e., the LCM, via a coarse-graining procedure. This procedure pinpoints
183 the missing dynamics in the LCM when compared to DG-FEM. Subsequently, the Mori-
184 Zwanzig (MZ) formalism is employed to determine the model form for the missing dynamics
185 in PIROM. Lastly, the data-driven identification of the missing dynamics in PIROM is
186 presented.

¹⁸⁷ **3.1 Deriving the Reduced-Physics Model via Coarse-Graining**

¹⁸⁸ The LCM is derived from a full-order DG on a fine mesh via coarse graining. This pro-
¹⁸⁹ cess constraints the trial function space of a full-order DG model to a subset of piece-wise
¹⁹⁰ constants, so that the variables \mathbf{u} , matrices \mathbf{A} , \mathbf{B} , and \mathbf{C} , and forcing vector \mathbf{f} are all ap-
¹⁹¹ proximated using a single state associated to the average temperature. The details of the
¹⁹² projection are described next.

¹⁹³ **3.1.1 Coarse-Graining of States**

¹⁹⁴ Consider a DG model as in eq. (8) for M elements and an LCM as in eq. (9) for N components;
¹⁹⁵ clearly $M \gg N$. Let $\mathcal{V}_j = \{i | E_i \in \Omega_j\}$ be the indices of the elements belonging to the j -th
¹⁹⁶ component, so $E_i \in \Omega_j$ for all $i \in \mathcal{V}_j$. The number of elements in the j -th component is $|\mathcal{V}_j|$.
¹⁹⁷ The average temperature on Ω_j is,

$$\bar{u}_j = \frac{1}{|\Omega_j|} \sum_{i \in \mathcal{V}_j} \int_{E^{(i)}} \boldsymbol{\phi}^{(i)}(x)^T \mathbf{u}^{(i)} d\Omega = \frac{1}{|\Omega_j|} \sum_{i \in \mathcal{V}_j} |E_i| \boldsymbol{\varphi}_i^{j\top} \mathbf{u}^{(i)}, \quad j = 1, 2, \dots, N \quad (15)$$

¹⁹⁸ where $|\Omega_j|$ and $|E_i|$ denote the area ($d = 2$) or volume ($d = 3$) of component j and element
¹⁹⁹ i , respectively. The orthogonal basis functions are defined as $\boldsymbol{\varphi}_i^{j\top} = [1, 0, \dots, 0]^\top \in \mathbb{R}^P$.

²⁰⁰ Conversely, given the average temperatures of the N components, $\bar{\mathbf{u}}$, the states of an
²⁰¹ arbitrary element E_i is written as,

$$\mathbf{u}^{(i)} = \sum_{k=1}^N \boldsymbol{\varphi}_i^k \bar{u}_k + \delta \mathbf{u}^{(i)}, \quad i = 1, 2, \dots, M \quad (16)$$

²⁰² where $\boldsymbol{\varphi}_i^k = 0$ if $i \notin \mathcal{V}_k$, and $\delta \mathbf{u}^{(i)}$ represents the deviation from the average temperature and
²⁰³ satisfies the orthogonality condition $\boldsymbol{\varphi}_i^k \boldsymbol{\varphi}_i^{j\top} = 0$ for all k .

²⁰⁴ Equations eqs. (15) and (16) are combined and written in matrix form as,

$$\bar{\mathbf{u}} = \boldsymbol{\Phi}^+ \mathbf{u}, \quad \mathbf{u} = \boldsymbol{\Phi} \mathbf{u} + \delta \mathbf{u} \quad (17)$$

²⁰⁵ where $\boldsymbol{\Phi} \in \mathbb{R}^{MP \times N}$ is a matrix of $M \times N$ blocks, with the (i, j) -th block as $\boldsymbol{\varphi}_i^j$, $\boldsymbol{\Phi}^+ \in \mathbb{R}^{N \times MP}$
²⁰⁶ is the left inverse of $\boldsymbol{\Phi}$, with the (i, j) -th block as $\boldsymbol{\varphi}_i^{j+} = \frac{|E_i|}{|\Omega_j|} \boldsymbol{\varphi}_i^{j\top}$, and $\delta \mathbf{u}$ is the collection of
²⁰⁷ deviations. By their definitions, $\boldsymbol{\Phi}^+ \boldsymbol{\Phi} = \mathbf{I}$ and $\boldsymbol{\Phi}^+ \delta \mathbf{u} = \mathbf{0}$.

208 **3.1.2 Coarse-Graining of Dynamics**

209 Next, consider a function of states in the form of $\mathbf{M}(\mathbf{u})\mathbf{g}(\mathbf{u})$, where $\mathbf{g} : \mathbb{R}^{MP} \rightarrow \mathbb{R}^{MP}$
210 is a vector-valued function, and $\mathbf{M} : \mathbb{R}^{MP} \rightarrow \mathbb{R}^{p \times MP}$ is a matrix-valued function with an
211 arbitrary dimension p . Define the projection matrix $\mathbf{P} = \Phi\Phi^+$ and the projection operator
212 \mathcal{P} as,

$$\begin{aligned}\mathcal{P}[\mathbf{M}(\mathbf{u})\mathbf{g}(\mathbf{u})] &= \mathbf{M}(\mathbf{P}\mathbf{u})\mathbf{g}(\mathbf{P}\mathbf{u}) \\ &= \mathbf{M}(\Phi\bar{\mathbf{u}})\mathbf{g}(\Phi\bar{\mathbf{u}})\end{aligned}\quad (18)$$

213 so that the resulting function depends only on the average temperatures $\bar{\mathbf{u}}$. Correspondingly,
214 the residual operator $\mathcal{Q} = \mathcal{I} - \mathcal{P}$, and $\mathcal{Q}[\mathbf{M}(\mathbf{u})\mathbf{g}(\mathbf{u})] = \mathbf{M}(\mathbf{u})\mathbf{g}(\mathbf{u}) - \mathbf{M}(\Phi\bar{\mathbf{u}})\mathbf{g}(\Phi\bar{\mathbf{u}})$. When
215 the function is not separable, the projection operator is simply defined as $\mathcal{P}[\mathbf{g}(\mathbf{u})] = \mathbf{g}(\mathbf{P}\mathbf{u})$.

216 Subsequently, the operators defined above are applied to coarse-grain the dynamics. First,
217 write the DG-FEM in eq. (8) as,

$$\dot{\mathbf{u}} = \mathbf{A}(\mathbf{u})^{-1}\mathbf{B}(\mathbf{u})\mathbf{u} + \mathbf{A}(\mathbf{u})^{-1}\mathbf{C}(\mathbf{u})\mathbf{u} + \mathbf{A}(\mathbf{u})^{-1}\mathbf{f}(t) \quad (19)$$

218 and multiply both sides by Φ^+ to obtain,

$$\Phi^+\dot{\mathbf{u}} = \Phi^+(\Phi\bar{\mathbf{u}} + \delta\dot{\mathbf{u}}) = \dot{\bar{\mathbf{u}}} = \Phi^+\mathbf{r}(\mathbf{u}, t) \quad (20)$$

219 Apply the projection operator \mathcal{P} and the residual operator \mathcal{Q} to the right-hand side to obtain,

$$\dot{\bar{\mathbf{u}}} = \mathcal{P}[\Phi^+\mathbf{r}(\mathbf{u}, t)] + \mathcal{Q}[\Phi^+\mathbf{r}(\mathbf{u}, t)] \equiv \mathbf{r}^{(1)}(\mathbf{u}, t) + \mathbf{r}^{(2)}(\mathbf{u}, t) \quad (21)$$

220 where $\mathbf{r}^{(1)}(\mathbf{u}, t)$ is resolved dynamics that depends on $\bar{\mathbf{u}}$ only, and $\mathbf{r}^{(2)}(\mathbf{u}, t)$ is the un-resolved
221 or residual dynamics. Detailed derivations and analysis of $\mathbf{r}^{(1)}(\mathbf{u}, t)$ and $\mathbf{r}^{(2)}(\mathbf{u}, t)$ can be
222 found in the Appendix.

223 It follows from Ref. [x] that the resolved dynamics is exactly the LCM, where the advection
224 term reduces to zero, i.e., $\bar{\mathbf{C}}(\bar{\mathbf{u}}) = \mathbf{0}$ as shown in the Appendix. Using the notation from
225 eq. (9), it follows that,

$$\begin{aligned}\mathbf{r}^{(1)}(\mathbf{u}, t) &= \bar{\mathbf{A}}(\bar{\mathbf{u}})^{-1}\bar{\mathbf{B}}(\bar{\mathbf{u}})\bar{\mathbf{u}} + \bar{\mathbf{A}}(\bar{\mathbf{u}})^{-1}\bar{\mathbf{C}}(\bar{\mathbf{u}})\bar{\mathbf{u}} + \bar{\mathbf{A}}(\bar{\mathbf{u}})^{-1}\bar{\mathbf{f}}(\bar{\mathbf{u}}) \\ &= \bar{\mathbf{A}}(\bar{\mathbf{u}})^{-1}\bar{\mathbf{B}}(\bar{\mathbf{u}})\bar{\mathbf{u}} + \bar{\mathbf{A}}(\bar{\mathbf{u}})^{-1}\bar{\mathbf{f}}(t)\end{aligned}\quad (22)$$

226 where the following relations hold,

$$\bar{\mathbf{A}}(\bar{\mathbf{u}}) = \mathbf{W} (\Phi^+ \mathbf{A} (\Phi \bar{\mathbf{u}})^{-1} \Phi)^{-1} \quad \bar{\mathbf{C}}(\bar{\mathbf{u}}) = \mathbf{0} \quad (23a)$$

$$\bar{\mathbf{B}}(\bar{\mathbf{u}}) = \mathbf{W} \Phi^+ \mathbf{B} (\Phi \bar{\mathbf{u}}) \Phi \quad \bar{\mathbf{f}}(t) = \mathbf{W} \Phi^+ \mathbf{f} \quad (23b)$$

227 where $\mathbf{W} \in \mathbb{R}^{N \times N}$ is a diagonal matrix with the i -th element as $[\mathbf{W}]_{ii} = |\mathcal{V}_k|$ if $i \in$
228 \mathcal{V}_k . As shown in the Appendix, the examination of the second residual term $\mathbf{r}^{(2)}(\mathbf{u}, t)$ in
229 eq. (21) reveals the physical sources of missing dynamics in the LCM: the approximation of
230 non-uniform temperature within each component as a constant, and the elimination of the
231 advection term due to coarse-graining.

232 In sum, the above results not only show that the LCM is a result of coarse-graining of
233 the full-order DG-FEM, but also reveal the discrepancies between the LCM and the DG-
234 FEM. In the subsequent section, the discrepancies will be corrected to produce the proposed
235 PIROM.

236 3.2 Formulation of Reduced-Order Model

237 The Mori-Zwanzig (MZ) formalism is an operator-projection technique used to derive ROMs
238 for high-dimensional dynamical systems, especially in statistical mechanics and fluid dynam-
239 ics Parish,Duraisamy . It provides an exact reformulation of the full-order dynamics in terms
240 of a subset of resolved variables. The proposed ROM is subsequently developed based on
241 such reformulation. Equation eq. (21) shows that the DG-FEM dynamics can be decomposed
242 into the resolved dynamics $\mathbf{r}^{(1)}(\mathbf{u}, t)$ and the orthogonal dynamics $\mathbf{r}^{(2)}(\mathbf{u}, t)$, in the sense of
243 $\mathcal{P}\mathbf{r}^{(2)} = 0$. In this case, the MZ formalism can be invoked to express the dynamics $\bar{\mathbf{u}}$ in terms
244 of $\bar{\mathbf{u}}$ alone as the projected Generalized Langevin Equation (GLE) Parish,Duraisamy ,

$$\dot{\bar{\mathbf{u}}}(t) = \mathbf{r}^{(1)}(\bar{\mathbf{u}}, t) + \int_0^t \tilde{\boldsymbol{\kappa}}(t, s, \bar{\mathbf{u}}) ds \quad (24)$$

245 where the first term is Markovian, and the integral term is referred to as the memory. The
246 integral term is non-Markovian, accounting for impact of past resolved states on the current
247 states through their interactions with the un-resolved states.

248 Next, to further inform the subsequent derivation of the ROM, the kernel $\tilde{\mathbf{k}}$ is examined
249 via a leading-order expansion, based on prior work x; this can be viewed as an analog of
250 zeroth-order holding in linear system theory with a sufficiently small time step. In this case,
251 the memory kernel is approximated as,

$$\tilde{\boldsymbol{\kappa}}(t, s, \bar{\mathbf{u}}) \approx \mathbf{r}^{(1)}(\bar{\mathbf{u}}, t) \cdot \nabla_{\bar{\mathbf{u}}} \mathbf{r}^{(2)}(\Phi \bar{\mathbf{u}}, t) \quad (25)$$

252 Note that the terms in $\mathbf{r}^{(1)}$ have a common factor $\bar{\mathbf{A}}^{-1}$; this motivates the following heuristic
253 modification of the model form in eq. (24),

$$\dot{\bar{\mathbf{u}}} = \mathbf{r}^{(1)}(\bar{\mathbf{u}}, t) + \bar{\mathbf{A}}^{-1}(\bar{\mathbf{u}}) \int_0^t \boldsymbol{\kappa}(t, s, \bar{\mathbf{u}}) ds \quad (26a)$$

$$\bar{\mathbf{A}}(\bar{\mathbf{u}})\dot{\bar{\mathbf{u}}} = \bar{\mathbf{B}}(\bar{\mathbf{u}})\bar{\mathbf{u}} + \bar{\mathbf{f}}(t) + \int_0^t \boldsymbol{\kappa}(t, s, \bar{\mathbf{u}}) ds \quad (26b)$$

254 where the original kernel $\tilde{\boldsymbol{\kappa}}$ is effectively normalized by $\bar{\mathbf{A}}^{-1}$. Intuitively, such choice of kernel
255 reduces its dependency on the averaged material properties, and simplifies the subsequent
256 design of model form.

257 Subsequently, the hidden states are introduced to “Markovianize” the system eq. (24).
258 In this manner, eq. (26b) is converted into a pure state-space model, with the functional
259 form of the LCM retained; since LCM is a physics-based model, then it encodes the phys-
260 ical information and retains explicit parametric dependence of the problem. Consider the
261 representation of the kernel as a finite sum of simpler functions, e.g., exponentials,

$$\boldsymbol{\kappa}(t, s, \bar{\mathbf{u}}) = \sum_{j=1}^m \mathcal{K}_j(t, s, \bar{\mathbf{u}}) [\mathbf{p}_j + \mathbf{d}_j(\bar{\mathbf{u}})] \phi_j(s, \bar{\mathbf{u}}) \quad (27)$$

262 where,

$$\mathcal{K}_j(t, s, \bar{\mathbf{u}}) = e^{-\int_s^t (\lambda_j + e_j(\bar{\mathbf{u}})) d\tau}, \quad \phi_j(s, \bar{\mathbf{u}}) = \mathbf{q}_j^\top \bar{\mathbf{u}}(s) + \mathbf{g}_j(\bar{\mathbf{u}})^\top \bar{\mathbf{u}}(s) + \mathbf{r}_j^\top \bar{\mathbf{f}}(s) \quad (28)$$

263 with suitable coefficients $\mathbf{p}_j, \mathbf{d}_j, \mathbf{q}_j, \mathbf{g}_j, \mathbf{r}_j \in \mathbb{R}^N$ and decay rates $\lambda_j, e_j(\bar{\mathbf{u}}) > 0$, that need to
264 be identified from data.

265 Define the hidden states as,

$$\beta_j(t) = \int_0^t \mathcal{K}_j(s, \bar{\mathbf{u}}) \phi_j(s, \bar{\mathbf{u}}) ds \quad (29)$$

266 then through its differentiation with respect to time,

$$\dot{\beta}_j(t) = -[\lambda_j + e_j(\bar{\mathbf{u}})] \beta_j(t) + \mathbf{q}_j^\top \bar{\mathbf{u}}(t) + \mathbf{g}_j(\bar{\mathbf{u}})^\top \bar{\mathbf{u}}(t) + \mathbf{r}_j^\top \bar{\mathbf{f}}(t) \quad (30)$$

267 and the memory term becomes,

$$\int_0^t \boldsymbol{\kappa}(t, s, \bar{\mathbf{u}}) ds = \sum_{j=1}^m [\mathbf{p}_j + \mathbf{d}_j(\bar{\mathbf{u}})] \beta_j(t) \quad (31)$$

268 Then, eq. (26b) is recast as the extended Markovian system,

$$\bar{\mathbf{A}}(\bar{\mathbf{u}})\dot{\bar{\mathbf{u}}} = \bar{\mathbf{B}}(\bar{\mathbf{u}})\bar{\mathbf{u}} + [\mathbf{P} + \mathbf{D}(\bar{\mathbf{u}})]\boldsymbol{\beta} + \bar{\mathbf{f}}(t) \quad (32a)$$

$$\boldsymbol{\beta} = [-\boldsymbol{\Lambda} + \mathbf{E}(\bar{\mathbf{u}})]\boldsymbol{\beta} + [\mathbf{Q} + \mathbf{G}(\bar{\mathbf{u}})]\bar{\mathbf{u}} + \mathbf{R}\bar{\mathbf{f}}(t) \quad (32b)$$

269 where,

$$\boldsymbol{\Lambda} = \text{diag}(\lambda_1, \lambda_2, \dots, \lambda_m) \in \mathbb{R}^{m \times m}, \quad \mathbf{P} = [\mathbf{p}_1, \mathbf{p}_2, \dots, \mathbf{p}_m] \in \mathbb{R}^{N \times m} \quad (33a)$$

$$\mathbf{D}(\bar{\mathbf{u}}) = [\mathbf{d}_1(\bar{\mathbf{u}}), \mathbf{d}_2(\bar{\mathbf{u}}), \dots, \mathbf{d}_m(\bar{\mathbf{u}})] \in \mathbb{R}^{N \times m}, \quad \mathbf{Q} = [\mathbf{q}_1, \mathbf{q}_2, \dots, \mathbf{q}_m] \in \mathbb{R}^{m \times N} \quad (33b)$$

$$\mathbf{G}(\bar{\mathbf{u}}) = [\mathbf{g}_1(\bar{\mathbf{u}}), \mathbf{g}_2(\bar{\mathbf{u}}), \dots, \mathbf{g}_m(\bar{\mathbf{u}})] \in \mathbb{R}^{m \times N}, \quad \mathbf{R} = [\mathbf{r}_1, \mathbf{r}_2, \dots, \mathbf{r}_m] \in \mathbb{R}^{m \times N} \quad (33c)$$

$$\mathbf{E}(\bar{\mathbf{u}}) = \text{diag}(e_1(\bar{\mathbf{u}}), e_2(\bar{\mathbf{u}}), \dots, e_m(\bar{\mathbf{u}})) \in \mathbb{R}^{m \times m} \quad (33d)$$

270 Since the hidden states $\boldsymbol{\beta}$ serve as the memory, their initial conditions are set to zero, i.e.,
271 $\boldsymbol{\beta}(t_0) = \mathbf{0}$, no memory at the beginning. The physics-infused model in eq. (32) retains the
272 structure of the LCM, while the hidden states account for missing physics through corrections
273 to the stiffness and advection matrices, as well as the forcing term.

274 Lastly, denote the collection of resolved and hidden states as $\mathbf{y} = [\bar{\mathbf{u}}, \boldsymbol{\beta}]^T \in \mathbb{R}^{n_y}$ with
275 $n_y = N + m$, then the proposed PIROM is summarized as,

$$\tilde{\mathbf{A}}\dot{\mathbf{y}} = [\tilde{\mathbf{B}} + \tilde{\mathbf{C}}]\mathbf{y} + \mathbf{H}\bar{\mathbf{f}}(t) \quad (34a)$$

$$\mathbf{z} = \mathbf{M}\mathbf{y} \quad (34b)$$

276 where,

$$\tilde{\mathbf{A}} = \begin{bmatrix} \bar{\mathbf{A}}(\bar{\mathbf{u}}) & \mathbf{O} \\ \mathbf{O} & \mathbf{I} \end{bmatrix} \in \mathbb{R}^{n_y \times n_y}, \quad \tilde{\mathbf{B}} = \begin{bmatrix} \bar{\mathbf{B}}(\bar{\mathbf{u}}) & \mathbf{P} \\ \mathbf{Q} & -\boldsymbol{\Lambda} \end{bmatrix} \in \mathbb{R}^{n_y \times n_y}, \quad \tilde{\mathbf{C}} = \begin{bmatrix} \mathbf{0} & \mathbf{D}(\bar{\mathbf{u}}) \\ \mathbf{G}(\bar{\mathbf{u}}) & \mathbf{E}(\bar{\mathbf{u}}) \end{bmatrix} \in \mathbb{R}^{n_y \times n_y}, \quad (35a)$$

$$\mathbf{H} = \begin{bmatrix} \mathbf{I} \\ \mathbf{R} \end{bmatrix} \in \mathbb{R}^{n_y \times N}, \quad \mathbf{M} \in \mathbb{R}^{n_z \times n_y} \quad (35b)$$

277 In eq. (34), the terms $\tilde{\mathbf{A}}$, $\tilde{\mathbf{B}}$, and $\bar{\mathbf{f}}$ are the LCM terms. The collection of matrices,

$$\boldsymbol{\Theta} = \{\mathbf{P}, \mathbf{D}(\bar{\mathbf{u}}), \mathbf{G}(\bar{\mathbf{u}}), \boldsymbol{\Lambda}, \mathbf{E}(\bar{\mathbf{u}}), \mathbf{Q}, \mathbf{G}(\bar{\mathbf{u}}), \mathbf{R}, \mathbf{M}\} \in \mathbb{R}^{n_\theta} \quad (36)$$

278 are learnable parameters to capture the memory effects. Particularly, the matrices \mathbf{P} , $\boldsymbol{\Lambda}$, \mathbf{Q} , \mathbf{R}
279 are constants that need to be identified from data, and account for the effects of coarse-
280 graining on the stiffness and forcing matrices. The matrices $\mathbf{D}(\bar{\mathbf{u}})$, $\mathbf{E}(\bar{\mathbf{u}})$, $\mathbf{G}(\bar{\mathbf{u}})$ are state-

281 dependent matrices, and account for the effects of coarse-graining on the advection matrix.
282 Leveraging the DG-FEM formula for the advection matrix in eq. (45c) in the Appendix, and
283 noting that the mesh displacements are functions of the ablating velocity as in eq. (4), the
284 state-dependent matrices for the i -th component are written as,

$$\mathbf{D}^{(i)}(\bar{\mathbf{u}}) \approx f^{(i)}(\bar{u}^{(i)})\mathbf{D}^{(i)}, \quad \mathbf{E}^{(i)}(\bar{\mathbf{u}}) \approx f^{(i)}(\bar{u}^{(i)})\mathbf{E}^{(i)}, \quad \mathbf{G}^{(i)}(\bar{\mathbf{u}}) \approx f^{(i)}(\bar{u}^{(i)})\mathbf{G}^{(i)} \quad (37)$$

285 where $f^{(i)}(\bar{u}^{(i)})$ is the surface recession velocity function in eq. (13) for the i -th component,
286 and $\mathbf{D}^{(i)}, \mathbf{E}^{(i)}, \mathbf{G}^{(i)}$ are constant matrices to be identified from data. In eq. (34), \mathbf{M} is a
287 fully-populated matrix that extracts the observables, i.e., the surface temperatures, from
288 the PIROM states \mathbf{y} . The PIROM incorporates explicit information on the temperature-
289 dependent material properties through the LCM matrices, as well as the surface recession
290 velocity function through eq. (37). The next step is focused on identifying the unknown
291 parameters Θ characterizing the hidden dynamics.

292 3.3 Learning the Hidden Dynamics from Data

293 The learning of the PIROM is achieved through a neural-ODE like approach [Chen2018](#).
294 For ease of presentation, consider the following compact form of the PIROM in eq. (34),

$$\mathcal{F}(\dot{\mathbf{y}}, \mathbf{y}; \boldsymbol{\xi}, \Theta) = \mathbf{0} \quad (38)$$

295 where $\boldsymbol{\xi}$ defines the parametrization of the problem, i.e., operating conditions, such as the
296 BC's, as well as the material properties. Consider a dataset of N_s high-fidelity trajectories
297 of observables over a time interval $[t_0, t_f]$,

$$\mathcal{D} = \left\{ \left(t_k, \mathbf{z}_{\text{HF}}^{(l)}(t_k), \boldsymbol{\xi}^{(l)} \right) \right\}_{l=1}^{N_s}, \quad k = 0, 1, \dots, K \quad (39)$$

298 The learning problem is formulated as the following differentially-constrained problem,

$$\min_{\Theta} \quad \frac{1}{N_s} \sum_{l=1}^{N_s} \frac{1}{K} \sum_{k=0}^K \left\| \mathbf{z}_{\text{HF}}^{(l)}(t_k) - \mathbf{M}\mathbf{y}^{(l)}(t_k) \right\|_2^2 \quad (40a)$$

$$\text{s.t.} \quad \mathcal{F} \left(\dot{\mathbf{y}}^{(l)}, \mathbf{y}^{(l)}; \boldsymbol{\xi}^{(l)}, \Theta \right) = \mathbf{0}, \quad t \in [t_0, t_f], \quad l = 1, 2, \dots, N_s \quad (40b)$$

$$\mathbf{y}^{(l)}(t_0) = \mathbf{y}_0(\boldsymbol{\xi}^{(l)}), \quad l = 1, 2, \dots, N_s \quad (40c)$$

299 **A Technical Details**

300 This appendix presents the technical details of the PIROM framework applied to the TPS
301 ablation problem. The first section provides the mathematical details for the definition of
302 the DG-FEM. The second section follows the projection procedures from Ref. x, and demon-
303 strates the effects of coarse-graining on the advection matrix. The third section presents the
304 derivation of the LCM model from an energy-conservation perspective.

305 **A.1 Full-Order Model**

306 To obtain the full-order numerical solution, the governing equation is spatially discretized
307 using variational principles of Discontinuous Galerkin (DG) to result in a high-dimensional
308 system of ordinary differential equations (ODEs). The DG-FEM model is written in an
309 element-wise form, which is beneficial for subsequent derivations of the lower-order models.
310 Note that the choice of DG approach here is mainly for theoretical convenience in the sub-
311 sequent coarse-graining formulation. In the numerical results, the full-order TPS ablation
312 simulations is computed using standard FEM instead, and the equivalence between DG and
313 standard FEM is noted upon their convergence.

314 **A.1.1 Domain Discretization**

315 Consider a conforming mesh partition of the domain, as shown in Fig. DOMAIN, where each
316 element belongs to one and only one component. Denote the collection of all M elements
317 as $\{E_i\}_{i=1}^M$. To ease the description of the DG model, a graph structure is employed. The
318 elements are treated as vertices, the set of which is denoted $\mathcal{V} = \{m\}_{m=1}^M$. Two neighboring
319 elements, E_i and E_j , are connected by an edge (i, j) , and the shared boundary between them
320 is denoted e_{ij} . The collection of all edges are denoted \mathcal{E} , and \mathcal{G} is referred to as a graph.
321 In the graph, the edges are unidirected, meaning if $(i, j) \in \mathcal{E}$ then $(j, i) \in \mathcal{E}$. Furthermore,
322 denote the neighbors of the i -th element as $\mathcal{N}_i = \{j | (i, j) \in \mathcal{E}\}$. Lastly, for the ease of
323 notation, introduce two special indices: T for the boundary of an element that overlaps with
324 the Dirichlet boundary condition, and similarly q for the Neumann boundary condition.

325 **A.1.2 Weak Form of Discontinuous Galerkin Method**

326 Choosing appropriate basis functions ϕ_k and ϕ_l and using the Interior Penalty Galerkin
 327 (IPG) scheme [3], the variational bilinear form for eq. (1a) is,

$$\sum_{i=1}^M a_{\epsilon,i}(\phi_k, \phi_l) = \sum_{i=1}^M L_i(\phi_k) \quad (41)$$

328 where ϵ is an user-specified parameter and,

$$a_{\epsilon,i}(\phi_k, \phi_l) = \int_{E^{(i)}} \left(\rho c_p \phi_k \frac{\partial \phi_l}{\partial t} + \nabla \phi_k \cdot (\mathbf{k} \nabla \phi_l) - \rho c_p \phi_k \mathbf{v} \cdot \nabla \phi_l \right) dE^{(i)} \quad (42a)$$

$$\begin{aligned} &= - \sum_{j \in \mathcal{N}_i \cup \{T_b\}} \int_{e_{ij}} \{ \mathbf{k} \nabla \phi_k \cdot n \} [\phi_l] de_{ij} + \epsilon \sum_{j \in \mathcal{N}_i \cup \{T_b\}} \int_{e_{ij}} \{ \mathbf{k} \nabla \phi_l \cdot n \} [\phi_k] de_{ij} \\ &\quad + \sigma \sum_{j \in \mathcal{N}_i \cup \{T_b\}} \int_{e_{ij}} [\phi_k] [\phi_l] de_{ij} \end{aligned} \quad (42b)$$

$$L_i(v) = \epsilon \sum_{j \in \mathcal{N}_i \cup \{T_b\}} \int_{e_{ij}} (\mathbf{k} \nabla \phi_l \cdot n) T_b de_{ij} + \int_{e_{iq}} \phi_k q_b de_{iq} + \sigma \int_{e_{iT}} \phi_k T_b de_{iT} \quad (42c)$$

329 In the bi-linear form above, the notations $[]$ and $\{\}$ are respectively the jumps and averages
 330 at the boundary e_{ij} share by two elements E_i and E_j ,

$$[u] = u|_{E_i} - u|_{E_j}, \quad \{u\} = \frac{1}{2} \left(u|_{E_i} + u|_{E_j} \right), \quad \text{for } x \in e_{ij} = E_i \cap E_j$$

331 Furthermore, in the bi-linear form, the terms associated with σ are introduced to enforce
 332 the Dirichlet boundary conditions; σ is a penalty factor whose value can depend on the size
 333 of an element. Depending on the choice of ϵ , the bi-linear form corresponds to symmetric
 334 IPG ($\epsilon = -1$), non-symmetric IPG ($\epsilon = 1$), and incomplete IPG ($\epsilon = 0$). All these schemes
 335 are consistent with the original PDE and have similar convergence rate with respect to mesh
 336 size. In the following derivations, the case $\epsilon = 0$ is chosen for the sake of simplicity.

337 **A.1.3 Discontinuous Galerkin Model**

338 Next, the DG-based model is written in an element-wise form. For the i -th element, use a
 339 set of P trial functions to represent the temperature as in eq. (6). Without loss of generality,
 340 the trial functions are assumed to be orthogonal, so that $\int_{E^{(i)}} \phi_k^{(i)}(x) \phi_l^{(i)}(x) dx = |E^{(i)}| \delta_{kl}$,
 341 where $|E^{(i)}|$ is the area ($n_d = 2$) or volume ($n_d = 3$) of the i -th element, and δ_{kl} is the
 342 Kronecker delta.

343 Using test functions same as trial functions, the dynamics $\mathbf{u}^{(i)}$ is obtained by evaluating

³⁴⁴ the element-wise bi-linear forms,

$$a_{\epsilon,i}(\phi_k^{(i)}, T^{(i)}) = L_i(\phi_k^{(i)}), \quad k = 1, 2, \dots, P \quad (43)$$

³⁴⁵ The above procedure yields,

$$\mathbf{A}^{(i)} \dot{\mathbf{u}}^{(i)} = (\mathbf{B}^{(i)} + \mathbf{C}^{(i)}(t)) \mathbf{u}^{(i)} + \sum_{j \in \mathcal{N}_i \cup \{T_b\}} \left(\mathbf{B}_{ij}^{(i)} \mathbf{u}^{(i)} + \mathbf{B}_{ij}^{(j)} \mathbf{u}^{(j)} \right) + \mathbf{f}^{(i)}(t) \quad (44)$$

³⁴⁶ where for $k, l = 1, 2, \dots, P$,

$$[\mathbf{A}^{(i)}]_{kl} = \int_{E^{(i)}} \rho c_p \phi_k^{(i)} \phi_l^{(i)} dE^{(i)} \quad (45a)$$

$$[\mathbf{B}^{(i)}]_{kl} = - \int_{E^{(i)}} (\nabla \phi_k^{(i)}) \cdot (\mathbf{k} \nabla \phi_l^{(i)}) dE^{(i)} \quad (45b)$$

$$[\mathbf{C}^{(i)}]_{kl} = \int_{E^{(i)}} \rho c_p \phi_k^{(i)} \mathbf{v}^{(i)} \cdot \nabla \phi_l^{(i)} dE^{(i)} \quad (45c)$$

$$[\mathbf{B}_{ij}^{(i)}] = \int_{e_{ij}} \left\{ \mathbf{k} \nabla \phi_k^{(i)} \cdot \hat{n} \right\} \phi_l^{(i)} - \sigma [\phi_k^{(i)}] \phi_l^{(i)} de_{ij} \quad (45d)$$

$$[\mathbf{B}_{ij}^{(j)}] = \int_{e_{ij}} - \left\{ \mathbf{k} \nabla \phi_k^{(i)} \cdot \hat{n} \right\} \phi_l^{(j)} + \sigma [\phi_k^{(i)}] \phi_l^{(j)} de_{ij} \quad (45e)$$

$$[\mathbf{f}^{(i)}]_k = \int_{e_{iq}} \phi_k^{(i)} q_b de_{iq} + \sigma \int_{e_{iT}} \phi_k^{(i)} de_{iT} \quad (45f)$$

³⁴⁷ The matrices $\mathbf{A}^{(i)} \in \mathbb{R}^{P \times P}$, $\mathbf{B}^{(i)} \in \mathbb{R}^{P \times P}$, and $\mathbf{C}^{(i)} \in \mathbb{R}^{P \times P}$ are respectively the capacitance,
³⁴⁸ conductivity, and advection matrices for element i . These matrices depend on ρ , c_p , \mathbf{k} , and
³⁴⁹ \mathbf{v} , and hence can be non-linear functions of $\mathbf{u}^{(i)}$. Since the trial functions are orthogonal, if
³⁵⁰ ρc_p is constant within an element, $\mathbf{A}^{(i)}$ is diagonal; otherwise, \mathbf{A}_i is symmetric and positive
³⁵¹ definite as $\rho c_p > 0$.

³⁵² For compactness, the element-wise model in eq. (44) is also written in matrix form,

$$\mathbf{A}(\dot{\mathbf{u}}) = [\mathbf{B}(\mathbf{u}) + \mathbf{C}(\mathbf{u})] \mathbf{u} + \mathbf{f}(t) \quad (46)$$

³⁵³ where $\mathbf{u} = [\mathbf{u}^{(1)}, \mathbf{u}^{(2)}, \dots, \mathbf{u}^{(M)}]^T \in \mathbb{R}^{MP}$ includes all DG variables, $\mathbf{f} = [\mathbf{f}^{(1)}, \mathbf{f}^{(2)}, \dots, \mathbf{f}^{(M)}]^T \in \mathbb{R}^{MP}$, \mathbf{A} and \mathbf{C} are matrices of M diagonal blocks whose i -th blocks are $\mathbf{A}^{(i)}$ and $\mathbf{C}^{(i)}$, and
³⁵⁴ \mathbf{B} is a matrix of $M \times M$ blocks whose (i, j) -th block is,
³⁵⁵

$$\mathbf{B}_{ij} = \begin{cases} \mathbf{B}^{(i)} + \sum_{j \in \mathcal{N}_i \cup \{T_b\}} \mathbf{B}_{ij}^{(i)}, & i = j \\ \mathbf{B}_{ij}^{(j)}, & i \neq j \end{cases} \quad (47)$$

³⁵⁶ The dependency of \mathbf{A} , \mathbf{B} , and \mathbf{C} on \mathbf{u} is explicitly noted in eq. (46), which is the source of
³⁵⁷ non-linearity in the current TPS problem. Moreover, the mesh velocity \mathbf{v} varies with space
³⁵⁸ and time, and thus the advection matrix \mathbf{C} varies with time as a function of q_b .

³⁵⁹ A.2 Coarse-Graining of Dynamics

³⁶⁰ The LCM is obtained by coarse-graining the full-order DG-FEM. This coarse-graining proce-
³⁶¹ dure produces resolved $\mathbf{r}^{(1)}(\mathbf{u}, t)$ and residual $\mathbf{r}^{(2)}(\mathbf{u}, t)$ dynamics as in eq. (21). This section
³⁶² presents the detail derivations and magnitude analysis for the resolved and residual dynam-
³⁶³ ics.

³⁶⁴ A.2.1 Resolved Dynamics

³⁶⁵ Using eq. (18), the resolved dynamics is computed as follows,

$$\mathbf{r}^{(1)}(\mathbf{u}, t) = \mathcal{P} [\Phi^+ \mathbf{A}(\mathbf{u})^{-1} (\mathbf{B}(\mathbf{u})\mathbf{u} + \mathbf{C}(\mathbf{u})\mathbf{u} + \mathbf{f}(t))] \quad (48a)$$

$$\begin{aligned} &= \Phi^+ \mathbf{A}(\mathbf{Pu})^{-1} \mathbf{PB}(\mathbf{Pu}) \mathbf{Pu} + \Phi^+ \mathbf{A}(\mathbf{Pu})^{-1} \mathbf{PC}(\mathbf{Pu}) \mathbf{Pu} \\ &\quad + \Phi^+ \mathbf{A}(\mathbf{Pu})^{-1} \mathbf{Pf}(t, \mathbf{Pu}) \end{aligned} \quad (48b)$$

$$\begin{aligned} &= \underbrace{\Phi^+ \mathbf{A}(\Phi \bar{\mathbf{u}})^{-1} \Phi}_{\#1} \underbrace{\Phi^+ \mathbf{B}(\Phi \bar{\mathbf{u}}) \Phi \bar{\mathbf{u}}}_{\#2} + \Phi^+ \mathbf{A}(\Phi \bar{\mathbf{u}})^{-1} \Phi \underbrace{\Phi^+ \mathbf{C}(\Phi \bar{\mathbf{u}}) \Phi \bar{\mathbf{u}}}_{\#3} \\ &\quad + \Phi^+ \mathbf{A}(\Phi \bar{\mathbf{u}})^{-1} \Phi \underbrace{\Phi^+ \mathbf{f}(t, \Phi \bar{\mathbf{u}})}_{\#4} \end{aligned} \quad (48c)$$

³⁶⁶ Detailed derivations for the #1, #2, and #4 terms can be found in Ref. [x](#). The effects of
³⁶⁷ coarse-graining on the advection term #3 are analyzed next.

³⁶⁸ **Term #3** The $\mathbf{C}(\mathbf{u}) \in \mathbb{R}^{MP \times MP}$ matrix contains M diagonal of size $P \times P$, since the
³⁶⁹ basis functions are defined locally on each element. Therefore, $[\mathbf{C}(\mathbf{u})]_{ij} = \mathbf{0}$ for all $i \neq j$ with
³⁷⁰ $i, j = 1, 2, \dots, M$. It follows that for $k, l = 1, 2, \dots, N$,

$$[\Phi^+ \mathbf{C}(t, \Phi \bar{\mathbf{u}}) \Phi]_{kl} = \sum_{i=1}^M \sum_{j=1}^M \boldsymbol{\varphi}_i^{k+} [\mathbf{C}(t, \Phi \bar{\mathbf{u}})]_{ij} \boldsymbol{\varphi}_j^l \quad (49a)$$

$$= \sum_{i=1}^M \boldsymbol{\varphi}_i^{k+} [\mathbf{C}(t, \Phi \bar{\mathbf{u}})]_{ii} \boldsymbol{\varphi}_i^l \quad (49b)$$

$$= \sum_{i \in \mathcal{V}_k} \boldsymbol{\varphi}_i^{k+} [\mathbf{C}(t, \Phi \bar{\mathbf{u}})]_{ii} \boldsymbol{\varphi}_i^l \quad (49c)$$

³⁷¹ where in the second row, the fact that $[\mathbf{C}(\mathbf{u})]_{ij} = 0$ for all $i \neq j$ is used, and in the last row,
³⁷² the fact that $\varphi_i^{k+} = 0$ for all $i \notin \mathcal{V}_k$ is used. Now, considering that $[\mathbf{C}(\mathbf{u})]_{ii}$ has a $(1, 1)$ -th
³⁷³ zero element, i.e., $[C_{11}(t, \Phi\bar{\mathbf{u}})]_{ii} = 0$, and that if $k \neq l$ then $i \notin \mathcal{V}_l$ and thus $\varphi_i^l = \mathbf{0}$, it follows
³⁷⁴ that for some index $i \in \mathcal{V}_k$,

$$\varphi_i^{k+} [\mathbf{C}(t, \Phi\bar{\mathbf{u}})]_{ii} \varphi_i^l = \varphi_i^{k+} [\mathbf{C}(t, \Phi\bar{\mathbf{u}})]_{ii} \varphi_i^k = \frac{|E_i|}{|\Omega_k|} [C_{11}(t, \Phi\bar{\mathbf{u}})]_{ii} = 0 \quad (50)$$

³⁷⁵ The matrix $[\Phi^+ \mathbf{C}(t, \Phi\bar{\mathbf{u}}) \Phi]_{kl} = 0$ for all $k, l = 1, 2, \dots, N$, and thus,

$$\bar{\mathbf{C}}(t, \bar{\mathbf{u}}) = \Phi^+ \mathbf{C}(t, \Phi\bar{\mathbf{u}}) \Phi = \mathbf{0} \quad (51)$$

³⁷⁶ as indicated by the LCM in eq. (9).

³⁷⁷ A.2.2 Magnitude Analysis for Residual Dynamics

³⁷⁸ Next, the magnitude of the residual dynamics $\mathbf{r}^{(2)}(\mathbf{u}, t)$ is analyzed to pinpoint the missing
³⁷⁹ physics in the LCM. By definition,

$$\mathbf{r}^{(2)}(\mathbf{u}, t) = \dot{\bar{\mathbf{u}}} - \mathbf{r}^{(1)}(\bar{\mathbf{u}}, t) \quad (52a)$$

$$= \Phi^+ \mathbf{r}(\mathbf{u}, t) - \mathbf{r}^{(1)}(\mathbf{u}, t) \quad (52b)$$

$$\begin{aligned} &= \underbrace{\Phi^+ \mathbf{A}(\mathbf{u})^{-1} \mathbf{B}(\mathbf{u}) \mathbf{u} - \bar{\mathbf{A}}(\bar{\mathbf{u}})^{-1} \bar{\mathbf{B}}(\bar{\mathbf{u}}) \bar{\mathbf{u}}}_{\#1} + \underbrace{\Phi^+ \mathbf{A}(\mathbf{u})^{-1} \mathbf{C}(\mathbf{u}) \mathbf{u} - \bar{\mathbf{A}}(\bar{\mathbf{u}})^{-1} \bar{\mathbf{C}}(t, \bar{\mathbf{u}}) \bar{\mathbf{u}}}_{\#2} \\ &\quad + \underbrace{\Phi^+ \mathbf{A}(\mathbf{u})^{-1} \mathbf{f}(t) - \bar{\mathbf{A}}(\bar{\mathbf{u}})^{-1} \bar{\mathbf{f}}(t)}_{\#3} \end{aligned} \quad (52c)$$

³⁸⁰ The magnitude analysis for terms $\#1$ and $\#3$ can be found in Ref. [x](#). The analysis for term
³⁸¹ $\#2$ is presented next. Let $\mathbf{D}(\bar{\mathbf{u}}) = \mathbf{A}(\Phi\bar{\mathbf{u}})^{-1} \mathbf{P} \mathbf{C}(t, \Phi\bar{\mathbf{u}})$, then,

$$\Phi^+ \mathbf{A}(\mathbf{u})^{-1} \mathbf{C}(\mathbf{u}) \mathbf{u} - \bar{\mathbf{A}}(\bar{\mathbf{u}})^{-1} \bar{\mathbf{C}}(t, \bar{\mathbf{u}}) \bar{\mathbf{u}} \quad (53a)$$

$$= \Phi^+ \mathbf{A}(\mathbf{u})^{-1} \mathbf{C}(\mathbf{u}) \mathbf{u} - \Phi^+ \mathbf{A}(\Phi\bar{\mathbf{u}})^{-1} \mathbf{P} \mathbf{C}(t, \Phi\bar{\mathbf{u}}) \Phi \Phi^+ \mathbf{u} \quad (53b)$$

$$= \Phi^+ \mathbf{A}^{-1}(\mathbf{u}) \mathbf{C}(\mathbf{u}) \mathbf{u} - \Phi^+ \mathbf{D}(\bar{\mathbf{u}}) \Phi \Phi^+ \mathbf{u} \quad (53c)$$

$$(53d)$$

382 where $\mathbf{P} = \Phi\Phi^+$. Thus,

$$\|\Phi^+\mathbf{A}(\mathbf{u})^{-1}\mathbf{C}(\mathbf{u})\mathbf{u} - \bar{\mathbf{A}}^{-1}(\bar{\mathbf{u}})\bar{\mathbf{C}}(t, \bar{\mathbf{u}})\bar{\mathbf{u}}\| \quad (54a)$$

$$\leq \|\Phi^+\mathbf{A}^{-1}(\mathbf{u})\mathbf{C}(\mathbf{u})\mathbf{u} - \Phi^+\mathbf{D}(\bar{\mathbf{u}})\mathbf{u}\| + \|\Phi^+\mathbf{D}(\bar{\mathbf{u}})\mathbf{u} - \Phi^+\mathbf{D}(\bar{\mathbf{u}})\Phi\Phi^+\mathbf{u}\| \quad (54b)$$

$$\leq \|\Phi^+\| \underbrace{\|\mathbf{A}^{-1}(\mathbf{u})\mathbf{C}(\mathbf{u})\mathbf{u} - \mathbf{D}(\bar{\mathbf{u}})\mathbf{u}\|}_{\#1} + \|\Phi^+\mathbf{D}(\bar{\mathbf{u}})\| \underbrace{\|\mathbf{u} - \Phi\Phi^+\mathbf{u}\|}_{\#2} \quad (54c)$$

383 where term $\#2$ is due to the approximation of non-uniform temperature as constants, and
 384 term $\#1$ is the error in the advection dynamics due to coarse-graining.

385 A.3 Lumped Capacitance Model

386 The following assumptions are employed: (1) the temperature in component (i) is described
 387 by a scalar time-varying average temperature $\bar{u}^{(i)}$, (2) between neighboring components (i)
 388 and (j) the heat flux is approximated as,

$$q_{ij} = \frac{\bar{u}^{(j)} - \bar{u}^{(i)}}{R_{ij}} \quad (55)$$

389 where R_{ij} is the thermal resistance. Empirically, for a component of isotropic heat conduction
 390 conductivity k , length ℓ , and cross-section area A , the thermal resistance is $R = \ell/kA$. Between
 391 components i and j , define $R_{ij} = R_i + R_j$. In addition, the heat flux due to Dirichlet
 392 boundary condition is computed as $q_{iT} = (T_b - \bar{u}^{(i)})/R_i$.

393 At component i , the dynamics of LCM are given by,

$$\int_{E^{(i)}} \rho c_p \dot{\bar{u}}^{(i)} dE^{(i)} = \left(\sum_{j \in \mathcal{N}_i} \int_{e_{ij}} \frac{\bar{u}^{(j)} - \bar{u}^{(i)}}{R_{ij}} de_{ij} \right) + \int_{e_{iq}} q_b de_{iq} + \int_{e_{iT}} \frac{T_b - \bar{u}^{(i)}}{R_i} de_{iT} \quad (56a)$$

$$\bar{A}^{(i)} \dot{\bar{u}}^{(i)} = \left(\sum_{j \in \mathcal{N}_i} \frac{|e_{ij}|}{R_{ij}} (\bar{u}^{(j)} - \bar{u}^{(i)}) \right) + |e_{iq}| \bar{q}^{(i)} + \frac{|e_{iT}|}{R_i} (\bar{T}^{(i)} - \bar{u}^{(i)}) \quad (56b)$$

$$= \sum_{j \in \mathcal{N}_i} \left(-\frac{|e_{ij}|}{R_{ij}} \bar{u}^{(i)} + \frac{|e_{ij}|}{R_{ij}} \bar{u}^{(j)} \right) + \left(-\frac{|e_{iT}|}{R_i} \bar{u}^{(i)} \right) + \left(|e_{iq}| \bar{q}^{(i)} + \frac{|e_{iT}|}{R_i} \bar{T}^{(i)} \right) \quad (56c)$$

$$= \sum_{j \in \mathcal{N}_i \cup \{T_b\}} \left(\bar{B}_{ij}^{(i)} \bar{u}^{(i)} + \bar{B}_{ij}^{(j)} \bar{u}^{(j)} \right) + \bar{f}^{(i)} \quad (56d)$$

394 where in eq. (56b) $|e|$ denotes the length ($d = 2$) or area ($d = 3$) of a component boundary
 395 e . The $\bar{A}^{(i)}$, $\bar{B}_{ij}^{(i)}$, and $\bar{B}_{ij}^{(j)}$ quantities are provided in eq. (12).

396 The lumped-mass representation for the four-component TPS is shown in Fig. 2. Let v_i

represent the area of the i -th element, $\overline{\rho c_p}_i$, the heat capacity evaluated using the average temperature $\bar{u}^{(i)}$, and $1/R_{ij} = 1/R_i(\bar{u}^{(i)}) + 1/R_j(\bar{u}^{(j)})$ the equivalent thermal resistance between elements i and j . Leveraging the formulas from eqs. (11) and (12), the LCM matrices are given by,

$$\bar{\mathbf{A}} = \begin{bmatrix} \overline{\rho c_p}_1 v_1 & 0 & 0 & 0 \\ 0 & \overline{\rho c_p}_2 v_2 & 0 & 0 \\ 0 & 0 & \overline{\rho c_p}_3 v_3 & 0 \\ 0 & 0 & 0 & \overline{\rho c_p}_4 v_4 \end{bmatrix}, \quad (57a)$$

$$\bar{\mathbf{B}} = \begin{bmatrix} \frac{1}{R_{12}} + \frac{1}{R_{14}} & -\frac{1}{R_{12}} & 0 & -\frac{1}{R_{14}} \\ -\frac{1}{R_{12}} & \frac{1}{R_{12}} + \frac{1}{R_{24}} + \frac{1}{R_{23}} & -\frac{1}{R_{23}} & -\frac{1}{R_{24}} \\ 0 & -\frac{1}{R_{32}} & \frac{1}{R_{32}} + \frac{1}{R_{34}} & -\frac{1}{R_{34}} \\ -\frac{1}{R_{14}} & -\frac{1}{R_{24}} & -\frac{1}{R_{34}} & \frac{1}{R_{14}} + \frac{1}{R_{24}} + \frac{1}{R_{34}} \end{bmatrix}, \quad \bar{\mathbf{f}} = \begin{bmatrix} \bar{q}^{(1)} \\ \bar{q}^{(2)} \\ \bar{q}^{(3)} \\ 0 \end{bmatrix} \quad (57b)$$

References

- [1] Adam J. Amar, A. Brandon Oliver, Benjamin S. Kirk, Giovanni Salazar, and Justin Drob. Overview of the charring ablator response (char) code. In AIAA, editor, *AIAA Aviation Forum*, 2016.
- [2] Guy L. Bergel, Frank B. Beckwith, Gabriel J. de Frias, Kevin M. Manktelow, Mark T. Merewether, Scott T. Miller, Krishen J. Parmar, Timothy S. Shelton, Jesse T. Thomas, Jeremy T. Trageser, Benjamin T. Treweek, Michael V. Veilleux, and Ellen B. Wagman. *Sierra/SolidMechanics 5.6 User's Manual*, 2022.
- [3] Gary Cohen and Sébastien Pernet. *Finite Element and Discontinuous Galerkin Methods for Transient Wave Equations*. Springer Dordrecht, Le Chesnay and Toulouse France, 2018.